GT2024-125128

NASA HECC GEOMETRY AND PERFORMANCE REVIEW PART 1: VALIDATION OF A COMPUTATIONAL MODEL FOR THE VANELESS DIFFUSER CONFIGURATION WITH AS-MANUFACTURED IMPELLER GEOMETRY

Gregorio Robles Vega[1], Alec J. Bosshart[1], Michael Ni[1], Ron-Ho Ni[1]
[1]AeroDynamic Solutions Inc, San Ramon, CA

Herbert M. Harrison[2], Tammy Nguyen-Huynh[2,3]
[2]NASA Glenn Research Center, Cleveland, OH
[3]The Ohio State University, Columbus, OH

ABSTRACT

An investigation of the NASA High Efficiency Centrifugal Compressor (HECC) vaneless diffuser configuration was performed. This multipart investigation presents an extensive validation of the computational model against experimental data. The validated model was then used to explore the effects of geometric differences between the as-manufactured and design-intent impellers. Lastly, the validated model was used for comparison against an experimental tip clearance study.

Part I of the investigation focused on describing the HECC vaneless computational model and its validation against the experimental data published in GT2023-103128. To generate the model, a verification of the manufactured impeller was performed and was confirmed to match the impeller CAD. Section data from the impeller CAD, referred to as the As-Manufactured geometry, were used for development of the computational model. Steady RANS simulations utilizing the Wilcox K-Omega 98 turbulence model and a multiblock structured mesh were used to conduct a mesh convergence study. The resultant mesh was then used for simulations at both design-speed and off-design speed conditions. Due to the challenges and uncertainties regarding the HECC performance and geometry, the model was extensively validated for use in Parts 2 and 3 of the paper The simulations compared well to data in both 1D and 2D terms for the major performance metrics of efficiency, total pressure rise, and total temperature rise. Based on the observed results the model was deemed validated and was used in the latter two parts of the multipart investigation.

Keywords: centrifugal compressor, experiment, CFD

NOMENCLATURE

CPU	Central Processing Unit
GPU	Graphics Processing Unit
HECC	High Efficiency Centrifugal Compressor
TPR	Total Pressure Ratio
TTR	Total Temperature Ratio
RANS	Reynolds-Averaged Navier-Stokes

1. INTRODUCTION

Detailed open-source centrifugal compressor test cases are very scarce. Such cases require both a design that is representative of those used in industry applications as well as expensive and time-consuming test campaigns for extensive data acquisition. This information varies from reliable blade geometry definitions to precise and accurate experimental campaign results. Nonetheless, open-source test cases have a high value to industry, academia, and researchers once made available. They not only provide opportunities to better understand the physics and performance gains from design choices but also serve as validation tools.

This paper examines the computational modeling of one of the few open-source centrifugal compressor test cases available, the NASA High Efficiency Centrifugal Compressor (HECC). The focus of the work is on the vaneless diffuser configuration with the baseline metal inlet whose experimental dataset and a CAD file of the HECC geometry was first made publicly available in 2022 by Harrison et al. [1]. The work presented in this paper is Part I of a three-part work, and the primary objective of this manuscript is to establish confidence in the modeling approaches that will be used in the remaining two parts of the paper. The following sections will provide an overview of the geometry, experimental approach, and experimental results as well as a description of the computational modeling methodologies employed. Lastly, a rigorous comparison is made against the experimental data set to establish confidence in the simulations given the historical difficulty in predicting the performance of HECC. Finally, the flow features observed in the simulations are discussed.

1.1 HECC Background

The High Efficiency Centrifugal Compressor was developed to improve state-of-the-art technology in centrifugal compressors. Aggressive targets were established at the outset of the project with the intention of achieving designated performance metrics through incorporation of advanced,

unproven design techniques while also providing a detailed centrifugal compressor dataset to facilitate future work. The performance goals were to simultaneously increase the efficiency, work factor, and stall margin of the stage while also reducing the overall radius relative to the predecessor compressor, CC3 [2]. Impeller blade lean, bow, and leading edge/trailing edge shaping were extensively investigated to optimize the impeller exit flow and stability at the high loading/low backsweep necessitated by the design requirements. Analogous techniques were incorporated in the diffuser, including fillets at the hub and shroud, elliptic leading and trailing edges, and the incorporation of a splitter vane.

Though the design assessment of the vaned diffuser stage was promising, the resultant compressor fell short of the program goals for efficiency and stall margin – an occurrence not uncommon during the design of centrifugal compressor stages. A summary of the design-intent metrics at the operating condition with comparison to the measured results is provided in Table 1. A primary cause of the observed differences between the numerically calculated and measured performance of HECC has remained difficult to pinpoint. While predictive numerical simulations often fall short of the desired accuracy for capturing the performance of centrifugal compressors, post-test CFD conducted with the advantage of hindsight also tended to overestimate the total pressure ratio and efficiency of the HECC vaned diffuser configuration [2]. Unexpected impeller-diffuser interactions not accounted for in the design-stage steady state CFD, Reynolds number effects from running the experiment at less-than-atmospheric inlet total pressure, and possible misalignment of the diffuser splitter vane have all been proposed as contributors to the dissimilarity between simulations and measurements, but each only accounts for a portion of the observed differences.

TABLE 1. DESIGN TARGET AND MEASURED DATA FOR HECC VANED DIFFUSER STAGE [1].

Parameter	Target	Measured	Difference
Stage Pressure Ratio	4.0-5.0	4.68	-
Polytropic Efficiency, %	>88%	85.5	-2.5
Exit Mass Flow Rate, lb_m/sec	2.6-3.1	3.0	-
Loading Coefficient, $\Delta H0/U_2^2$	0.6-0.7	0.81	+0.11
Exit Swirl Angle, deg.	15°	34.3°	19.3°
Surge Margin, %	13%	7.5%	-5.5%

2. AS-MANUFACTURED IMPELLER GEOMETRY

To better understand the HECC impeller performance, a vaneless diffuser was designed as a follow-up effort to the original vaned diffuser stage [1]. The computational effort was refreshed with the simplified vaneless diffuser stage alongside the experimental measurement campaign. To begin, the impeller geometry was validated against a solid model used for fabrication of the stage and which was only made publicly

available in 2023 [1]. In addition to the original inspection conducted after delivery of the impeller, a coordinate measuring machine was used to validate that the solid model of the impeller was in agreement with the physical hardware. The greatest documented deviation of the fabricated impeller from the solid model occurred at the trailing edge of a main blade and splitter blade pair with differences of 0.0021-in 0.0033-in, respectively. At all other directly compared points, the fabricated impeller was within the 0.002-in single sided tolerance specification.

Having revalidated the impeller model against the fabricated hardware, blade sections were manually extracted from the 3D model. Fifteen approximately constant span slices were made along the impeller main blade and splitter blade pairs with a clustering of blade sections towards the base of the blades to capture the hub side fillets (Figure 1a and Figure 1b) and unique trailing edge shape (Figure 1b). The resultant blade sections are heretofore referred to as the "as-manufactured" impeller geometry. Since the solid model is a high-fidelity representation of the fabricated impeller geometry, the as-manufactured blade sections are also considered to be precise and reliable representations of the cold impeller geometry.
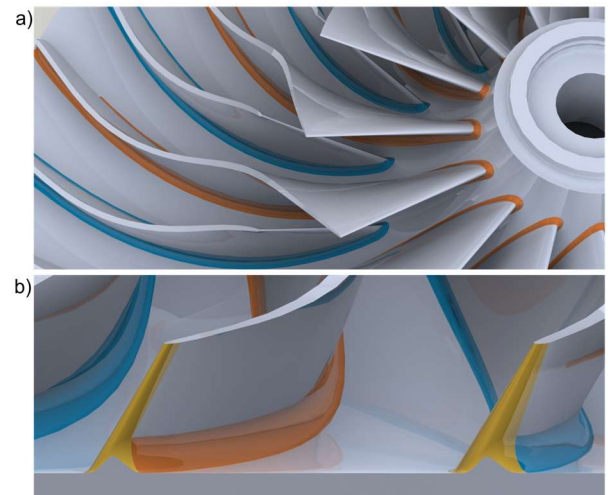

FIGURE 1. HECC IMPELLER WITH A/B) MAIN BLADE FILLETS, A/B) SPLITTER BLADE FILLETS, AND B) TRAILING EDGE SHAPING HIGHLIGHTED IN ORANGE, BLUE, AND YELLOW, RESPECTIVELY.

3. HECC VANELESS STAGE AND INSTRUMENTATION

The experimental data obtained for validation of the computational model in the present work were acquired with the High Efficiency Centrifugal Compressor vaneless diffuser configuration and the baseline metal inlet in the Small Engine Components Compressor Test Facility at NASA Glenn Research Center. A meridional view of the components and instrumentation relevant to the present work is given in Figure 2. The inlet duct conducts flow from the upstream settling chamber to the impeller. The vaneless diffuser downstream of the impeller recovers static pressure from the high kinetic energy impeller exit flow and turns the flow from radial to axial. After the radial-

to-axial bend, the flow is passed to a collector, through a throttle valve, and exhausted to atmosphere.

The impeller is geometrically scaled to approximately twice that of an engine axi-centrifugal compressor stage and has 15 main blade/splitter blade pairs. The diffuser is entirely vaneless from the impeller exit to the stage exit. The design rotational speed of the impeller is 21,789-rpm at standard day conditions. At 100% corrected speed and the design mass flow rate of 11-lbm/s, the vaneless stage and impeller provide total pressure ratios of 4.54 and 5.11, respectively. Additionally, at the design point the flow coefficient (φ) is 0.044 and the loading coefficient (ψ) is 0.79. The machine Mach number ($M_{U_2} = \frac{U_2}{\sqrt{\gamma R T_{00}}}$, where U_2 is the physical speed of the trailing edge radius) is approximately 1.45 at design speed, and the tip relative Mach Number is between 0.8 and 0.9 at all recorded points on the 100% characteristic. The design intent tip clearance is 0.012-in at the impeller trailing edge, or 2.0% of the trailing edge blade height. A full design report of the HECC vaned diffuser configuration is given by Medic et al. [2], and a review of the Small Engine Components Compressor Test Facility and the various HECC configurations as well as the vaneless diffuser stage experimental data are documented in detail by Harrison et al. [1].

Total pressure and total temperature are measured at three meridional locations identified in Figure 2: upstream of the inlet in the settling chamber (Station 0), downstream of the impeller (Station 3), and at the stage exit (Station 7). The total pressure and total temperature rakes at Station 3 are at a radius of 9.108-in (a radius ratio of 1.072 relative to the impeller trailing edge), and given their close proximity to the impeller exit, are used to quantify the impeller performance. In addition to the total quantities collected with stationary rakes, traversable probes may also be inserted through the casing at Station 3. Total temperature and 3-hole probes are used to obtain total temperature, total pressure, and flow angle measurements with a high degree of spanwise resolution at the impeller exit. Static pressures are distributed across both the hub and shroud of the stationary components as well as on the shroud over the impeller. Finally, capacitance probes record the impeller tip clearance at the inducer, knee, and exducer.

Steady pressure measurements within the primary flow path were recorded with Netscanner 9816 15-psid or 50-psid modules with uncertainties of 0.15%. The mass flow rate was calculated with an ASME standard orifice plate to within 1% uncertainty at all operating conditions. The orifice plate pressures were measured with Druck UNIK 5000 pressure transducers which have an uncertainty of 0.04%. Temperatures are quantified to within 4°F using K-type thermocouples connected Scanivalve DTS 4050 units. Rotational speed was maintained within 0.013% of the desired setpoint via feedback control from the variable frequency power system. All experimental aerodynamic data contained h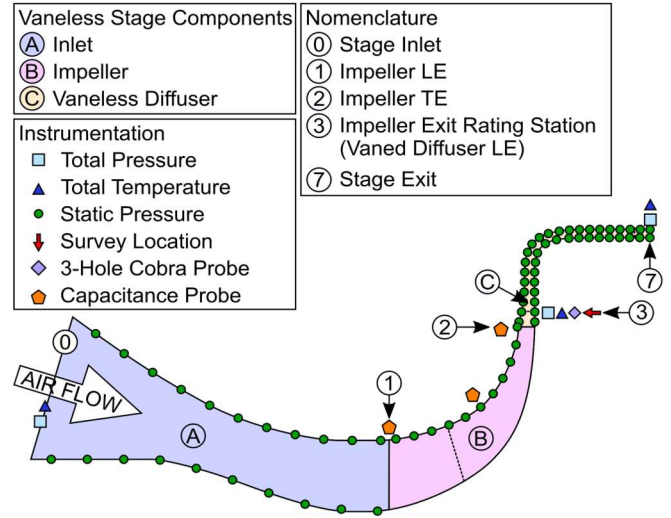erein have been made available on the HECC Data Archive at https://storage.googleapis.com/hecc-data/NASA-HECC-Data-Archive.zip [3].

FIGURE 2. HECC VANELESS DIFFUSER COMPONENTS, NOMENCLATURE, AND INSTRUMENTATION.

4. COMPUTATIONAL MODELING APPROACH
4.1 Solver Description: ADS CFD Code Leo
Code Leo is a density-based, compressible, explicit time-marching code flow solver. It uses the Ni-Scheme distribution formula that is 2nd order accurate in both time and space [4]. A blend of 2nd and 4th order smoothing is used to reduce the oscillation of the flowfield caused by shocks and transient flow. The solver can run on structured grids, unstructured grids or a mixture of both. The solver is also capable of running on both CPUs and GPUs. Both CPU and GPU solvers have the same capabilities and provide equivalent solutions. Moreover, the solver is HPC scalable using high speed MPI.

Code Leo is capable of running steady RANS, unsteady RANS (Non-Linear Harmonic Balance and Dual Time Stepping) [5,6,7], detached eddy simulations and large eddy simulations [8,9] on both CPUs and GPUs. Moreover, conjugate heat transfer [10] and flutter [11] capabilities are also available. Code Leo has been applied to compressors and turbines. This includes multi-stage machines as well as bypass/core flow simulations. Advanced simulations such as casing treatments and inlet distortion have also been demonstrated. Code Leo has also been applied to external aerodynamic applications including high-lift simulations, cruise conditions and VTOL simulations.

4.2 Model Domain and Mesh Generation
The model domain was split into four rows: inlet duct, impeller, vaneless diffuser and exit duct. The components and interfaces of the model are presented in Figure 3. The impeller exit corresponds to station 3 from the experiment. Similarly, the vaneless diffuser exit corresponds to station 7. All simulations used a steady RANS single passage. The inlet duct/impeller interface was set to a mixing plane approximation. Since the diffuser is vaneless, a frozen rotor approximation was used at the

impeller/diffuser interface to allow the wakes to propagate downstream. Lastly, the vaneless diffuser/exit duct interface used an interpolation (node-to-node) condition.
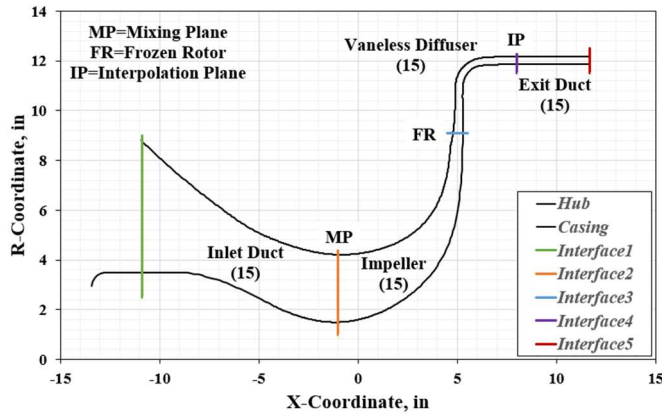

FIGURE 3. CROSS-SECTIONAL VIEW OF THE MODEL DOMAIN.

In regard to seal leakage flows, the experimental results were used to guide the decision to include leakage into the model or not. When reviewed, the experimental results in [3] showed minimal changes to the Stage TPR across the five speedlines for which data was measured when the lab seal differential pressure was set to 0.5psid and compared to 0.0psid. Thus, the incurred cost in model complexity from either meshing the leakage path or running a 1D leakage model was deemed unnecessary.

Surface roughness in the model was set so that the airfoil surfaces are hydraulically smooth. The model used is a sand grain roughness model detailed in [12]. When the specified sand grain roughness value is converted to its equivalent surface roughness, the value is reasonable compared to the measured surface roughness from the impeller.

Mesh generation was performed using ADS CFD Code Wand. Code Wand is an automated structured multi-block mesh generator. An OHH mesh topology with a tip cap mesh for the tip clearance region was used for the simulations. The mesh wall spacing for all mesh levels was 0.0001in. The resulting y+ values were approximately 1 for all cases. Thus, wall integration was used for all meshes. Lastly, adiabatic walls were used.

4.3 Aerodynamic Conditions and Solver Settings

The simulations used an inlet total pressure and total temperature of 14.7-psi and 518.7-°R, respectively. The impeller tip clearance was specified as a uniform value of 12mils. All simulations were executed using the Wilcox K-Omega 98 turbulence model and variable specific heat. The static pressure at the stage exit was varied using an automated iterative compressor speedline generator tool to march the simulation from choke to stall. The numerical stall point was determined to within 0.1% static pressure change. Simulations were executed on a laptop with 1 Nvidia RTX A5000 Mobile GPU and one simulation would complete 6,000 iterations (typical number of iterations required for case convergence) in approximately 7 minutes and 42 seconds.

4.4 Mesh Convergence Study

A mesh convergence study was performed to ensure that the mesh size selected for the investigation had reached mesh independence. Four mesh sizes were generated by increasing the number of planes in the axial, circumferential, and radial directions. Table 2 provides the details regarding the mesh level sizes. All four mesh densities were run at 8 different points along the speedline, though no attempt was made at this point to push towards numerical stall. Instead, the four mesh levels were each run to convergence (if possible) at eight exit static pressures. Out of the eight points that were executed, the two points closest to stall for the coarse mesh failed to converge. For all other mesh levels, only the point closest to stall failed to converge. The design speed characteristics resulting from the mesh convergence study are presented in Figure 4. Although there is a significant difference in the speedlines between the Coarse mesh and the more refined meshes, there is little change from the Medium to Very Fine mesh levels for stage TPR, TTR, and efficiency. In fact, the stage work input characteristics are nearly the exact same for the three more refined meshes in Figure 4b. The stage TPR speedlines are quite similar at the Fine and Very Fine mesh levels, which, in combination with the agreement in TTR, leads to a well-converged estimate of efficiency between the two highest grid densities. Since the difference between each of the parameters at all of the considered operating conditions is negligible between the Fine and Very Fine meshes, the solution was deemed to have reached mesh independence at the Fine mesh. As such, the Fine mesh was used for the proceeding analyses in Parts I, II, and III of the paper.

The Fine mesh has 45 radial planes (k-planes) across the span as well as 17 additional radial planes (k-planes) in the tip gap section. The main blade has 249 points around the airfoil, while the splitter blade has 169 points around the airfoil. The mesh at 50% span of the impeller is shown in Figure 5. Zoomed-in images of the leading and trailing edges can be seen in the lower two quadrant, and the top right quadrant shows a cut across the span. Fanouts were employed at both the leading and trailing edges of the impeller.

TABLE 2. COUNTS FOR THE MESH FAMILY USED FOR THE MESH CONVERGENCE STUDY.

|		# of Nodes	# of Elements	Total Nodes	Total Elements
Coarse	Inlet Duct	132,349	124,416	766,599	687,360
	Impeller	442,072	383,232		
	Vaneless Diffuser	117,845	110,592		
	Exit Duct	74,333	69,120		
Medium	Inlet Duct	242,433	230,400	1,313,887	1,208,320
	Impeller	706,308	632,320		
	Vaneless Diffuser	218,489	207,360		
	Exit Duct	146,657	138,240		
Fine	Inlet Duct	388,485	371,712	2,027,603	1,891,968
	Impeller	1,036,748	945,792		
	Vaneless Diffuser	353,565	337,920		
	Exit Duct	248,805	236,544		
Very Fine	Inlet Duct	537,089	516,096	2,794,519	2,630,400
	Impeller	1,404,732	1,297,152		
	Vaneless Diffuser	492,793	473,088		
	Exit Duct	359,905	344,064		

a)

b)

c)
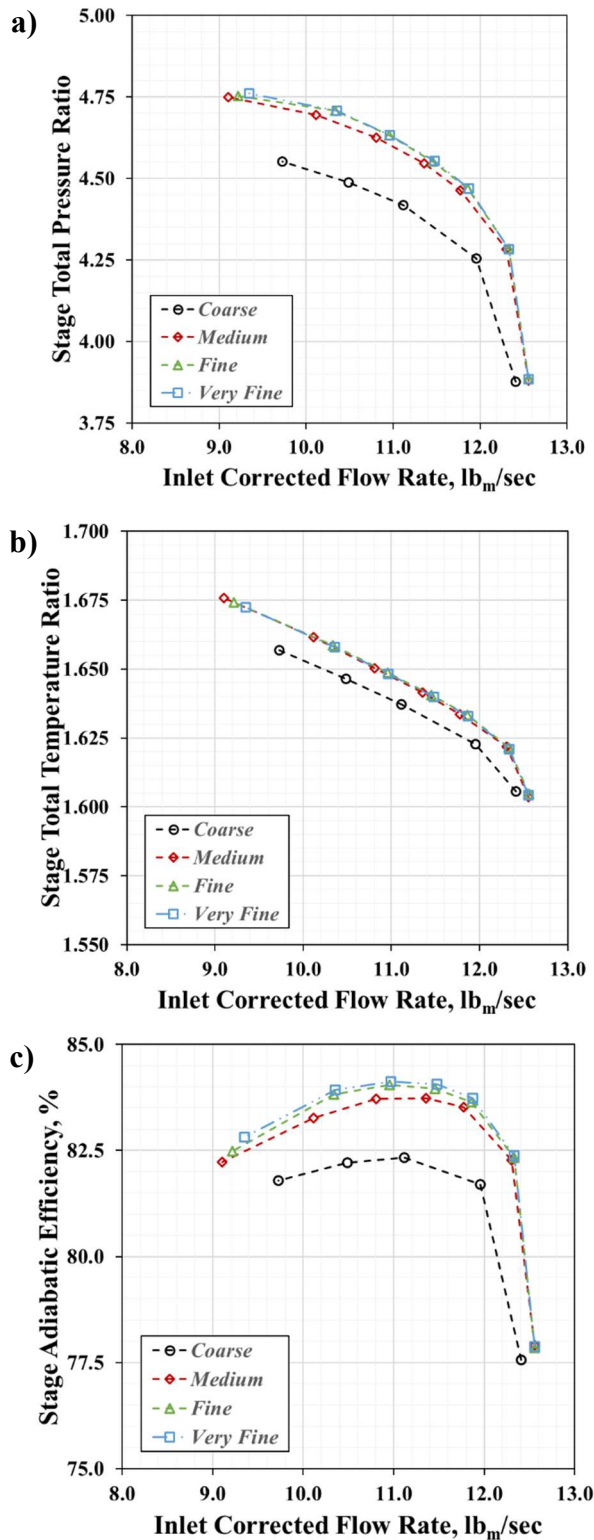
FIGURE 4. DESIGN SPEED CHARACTERISTIC FOR THE FOUR MESH DENSITIES: A) STAGE TPR, B) STAGE TTR, AND C) STAGE EFFICIENCY
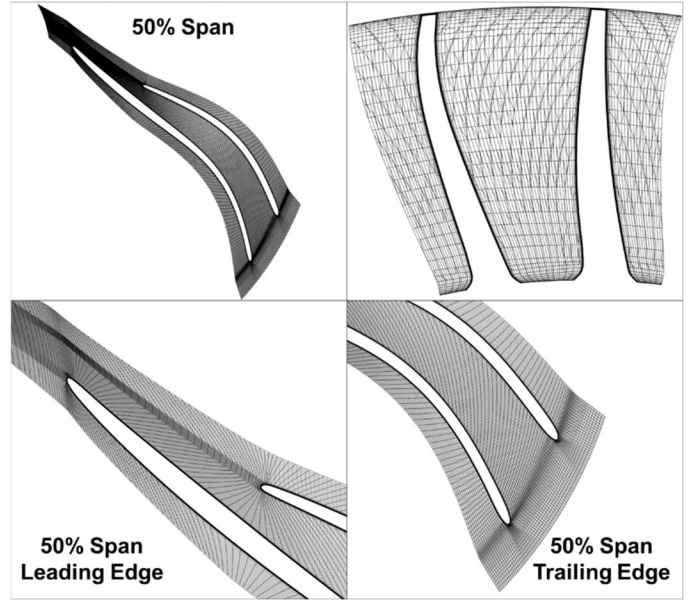

FIGURE 5. IMAGES OF THE FINE MESH AT 50% SPAN AND ACROSS THE SPAN.

5.   MODEL VALIDATION
5.1 One Dimensional Performance Metrics

The performance of the HECC vaneless diffuser configuration was considered at both the impeller exit (station 3) and the stage exit (station 7) to evaluate the efficacy of the numerical model from both a stage and component perspective. All numerical data has been compared to the Baseline Metal Inlet configuration of the HECC vaneless diffuser stage [1], denoted as the 2018 data (2018 being the year the data was acquired) for the remainder of the manuscript. The total temperature rakes at the impeller exit failed early in the experimental test campaign, so the comparisons at Station 3 in the present work are limited to total pressure.

All values provided for the CFD are mass averaged quantities. These mass averaged quantities are automatically generated by Code Leo. A comparison was made between the mass averaged 1D quantities and area averaged quantities post-processed in a similar manner as the experiment. The area averaged approach used five spanwise values to define station 3. The spanwise values were taken at 10%, 30%, 50%, 70% and 90% spans which corresponded to the rake element locations. Each used an area average weight coefficient of 20%. Station 7 used four spanwise locations at 12.6%, 37.8%,62.8% and 87.6%. The area average weight coefficient for the rake element locations were 25.5%, 25.1% 24.9% and 24.8%, respectively. The results showed the area averaging approach results in minimal differences in TPR when compared to the mass averaging approach as can be seen in Figure 6. Since the differences were minimal, mass averaging was used for the remaining results.
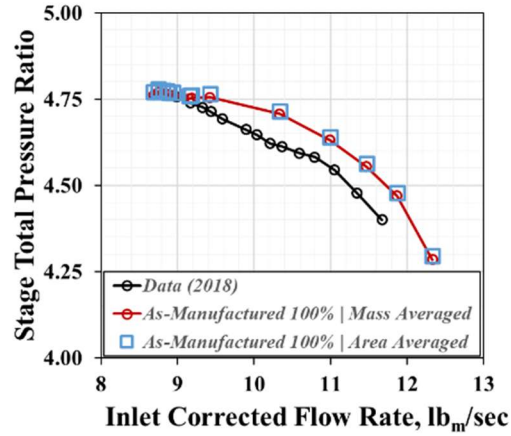
FIGURE 6. COMPARISON OF MASS AVERGAGED VS AREA AVERAGED POST-PROCESSING METHODS FOR THE 100% STAGE TOTAL PRESSURE RATIO.
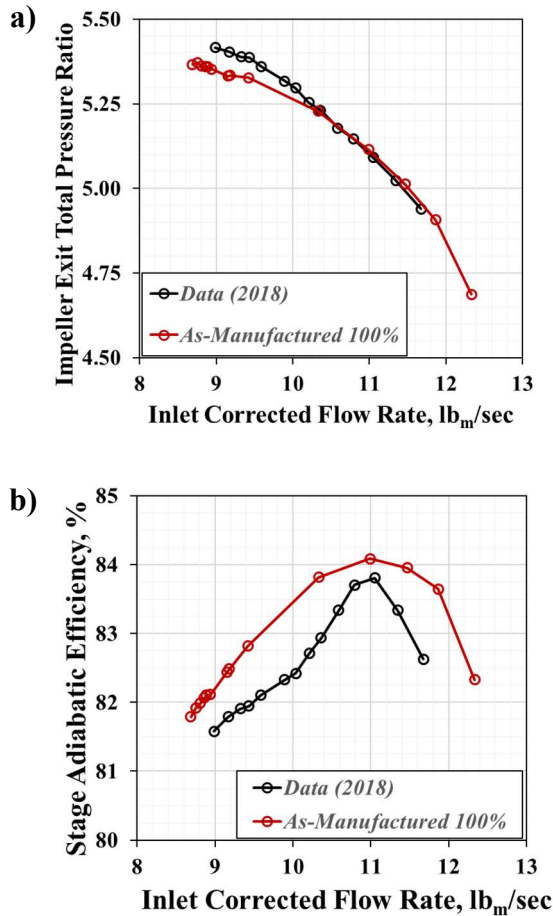

FIGURE 7. COMPARISON BETWEEN DATA AND AS-MANUFACTURED SIMULATIONS: A) IMPELLER EXIT TPR AND B) STAGE EFFICIENCY

Comparison of the 2018 data to the validated, as-manufactured model at 100% design speed shows good agreement in the impeller exit total pressure ratio, Figure 7a. The simulations show a slightly lower pressure rise near stall. All other locations show a good agreement in the shape and magnitude. At the design point (11lb_m/sec), the data and as-manufactured model show a percent difference of only 0.46%. In addition to accurately representing impeller TPR at 100% design speed, the as-manufactured model also showed good agreement with the measured stage efficiency (Figure 7b). At the design point, the stage total pressure ratio from the simulations is higher by 1.90 percent difference which indicates higher losses occurred in the experiment vaneless diffuser than were predicted by the simulation. At the design mass flow rate, the differences between stage total temperature ratio and stage efficiency were 0.69% and 0.33%, respectively. The values and percentage differences at the stage design point for both the experiment and model are compiled in Table 3.

The 1-D performance parameters were also compared at the off-design conditions: 95% design speed and 90% design speed. The results at these lower speeds again show good agreement with the experimental data, Figure 8. The impeller exit total pressure ratio shows similar trends to the observations made at 100% speed. The shape and magnitude of the speedlines is again captured very well near the operating point and open throttle. At near stall conditions the model predicts slightly less pressure rise but is still an adequate prediction. The stage total pressure ratio, stage total temperature ratio, and stage efficiency also show good agreement with the experimental data. Both the shapes and magnitudes align between the simulations and the experimental data. The simulations predict slightly higher pressure and temperature rise than those observed in the experiment, but the differences are of a percent difference less than those observed for the 100% speed design point. These differences lead to peak stage efficiency being higher by 0.13% and 0.41% for the 95% speed and 90% speed, respectively.

TABLE 3. 1-D PERFORMANCE PARAMETER AT THE DESIGN POINT FOR BOTH EXPERIMENTAL DATA AND AS-MANUFACTURED SIMULATIONS.

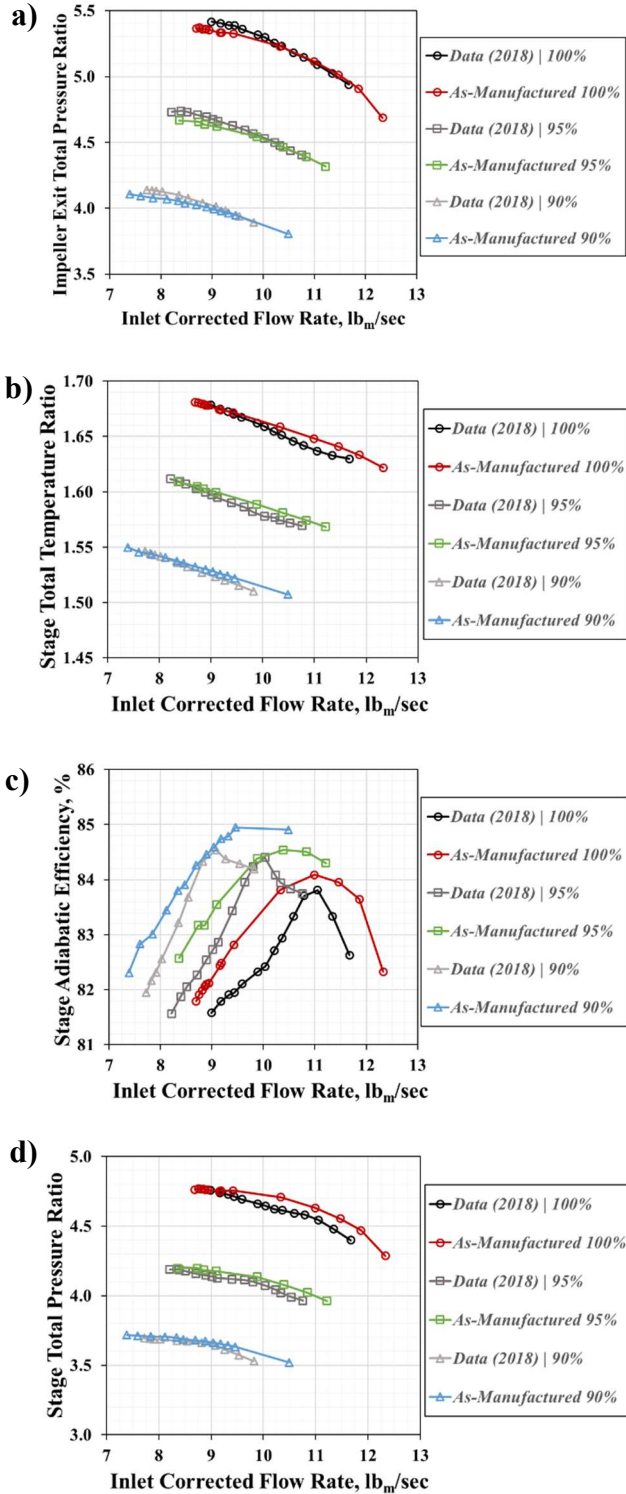| Parameter	Experiment	CFD	Percent Error, %
Inlet Corrected Flow Rate, lb_m/sec	11.05	10.99	-0.55
Impeller Exit TPR	5.091	5.115	0.46
Stage TPR	4.544	4.631	1.90
Stage TTR	1.637	1.648	0.69
Stage Efficiency, %	83.81	84.09	0.33

a)

b)

c)

d)

FIGURE 8. COMPARISON BETWEEN DATA AND AS-MANUFACTURED SIMULATIONS OF STAGE EFFICIENCY AT OFF-DESIGN CONDITIONS: A) IMPELLER EXIT TPR, B) STAGE TPR, C) STAGE TTR, AND D) STAGE EFFICIENCY

5.2 Spanwise Profiles at 100% Corrected Speed

To validate the model for not just overall performance but detailed flow analysis, as well, the numerically predicted spanwise flow properties were compared to those in the experiment. The profiles are again compared at both the impeller exit (station 3) and stage exit (station 7). Three points along the 100% speedline were selected: near choke, design point, and near stall, and three properties were compared at each of these points: impeller exit total pressure ratio, stage pressure ratio, stage temperature ratio. The experimental inlet corrected flow rates for the experimental points are $11.67 lb_m/sec$, $11.05 lb_m/sec$, and $8.99 lb_m/sec$, respectively. The corresponding points selected for comparison in the CFD simulations were at inlet corrected flow rates of $11.87 lb_m/sec$, $10.99 lb_m/sec$ and $8.94 lb_m/sec$, respectively.

Figure 9 shows the near choke, design point, and near stall impeller exit total pressure ratio profile comparisons. The impeller exit total pressure ratio profiles from the simulations align well with the shapes from the experiment at all operating conditions. As the compressor moves from near choke to near stall conditions the changes in the shapes and magnitudes are all correctly captured. Both the experimental data and the model show a bias in total pressure towards the tip with a peak TPR at approximately 70% span.

The next property that was compared was the stage total pressure ratio, again at near choke, design point, and near stall conditions (Figure 10). The simulation profiles from the model accurately capture the increases in pressure rise as the simulation moves from choke to stall. However, the shape of the experimental profile is biased towards the hub while the model shows a bias towards the tip. Thus, the 2-D profile predictions from the model are deemed to agree well in terms of magnitude but have an opposite trend in regard to the bias of the shape.

The final property that was compared was the stage total temperature ratio: Figure 11 shows the stage total temperature ratio profiles at near choke, design point, and near stall. The simulation profiles from the model accurately capture the increases in temperature rise as the simulation moves from choke to stall. However, similar to the stage total pressure ratio profiles, the shape of the experimental profile is biased towards the hub while the model shows a bias towards the tip. Thus, the 2-D profile predictions from the model are deemed to agree well with the observations from the experiment in terms of magnitude but show an opposite trend in regard to the bias of the shape.
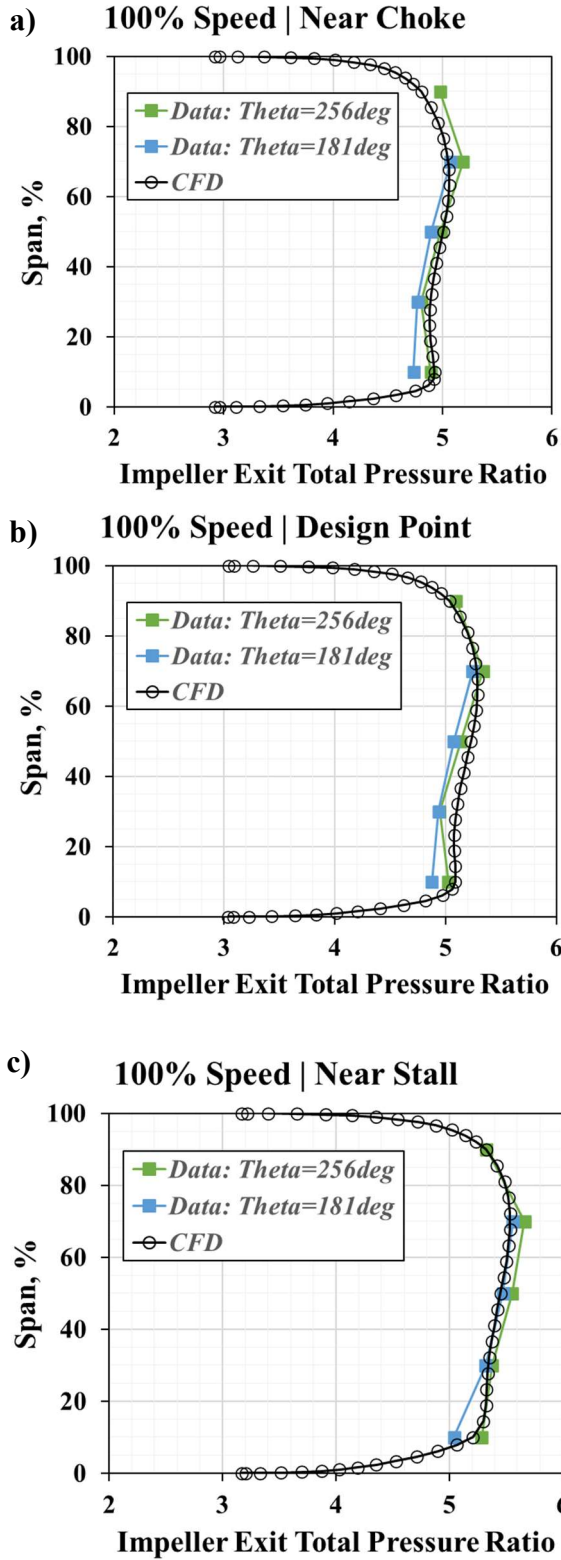
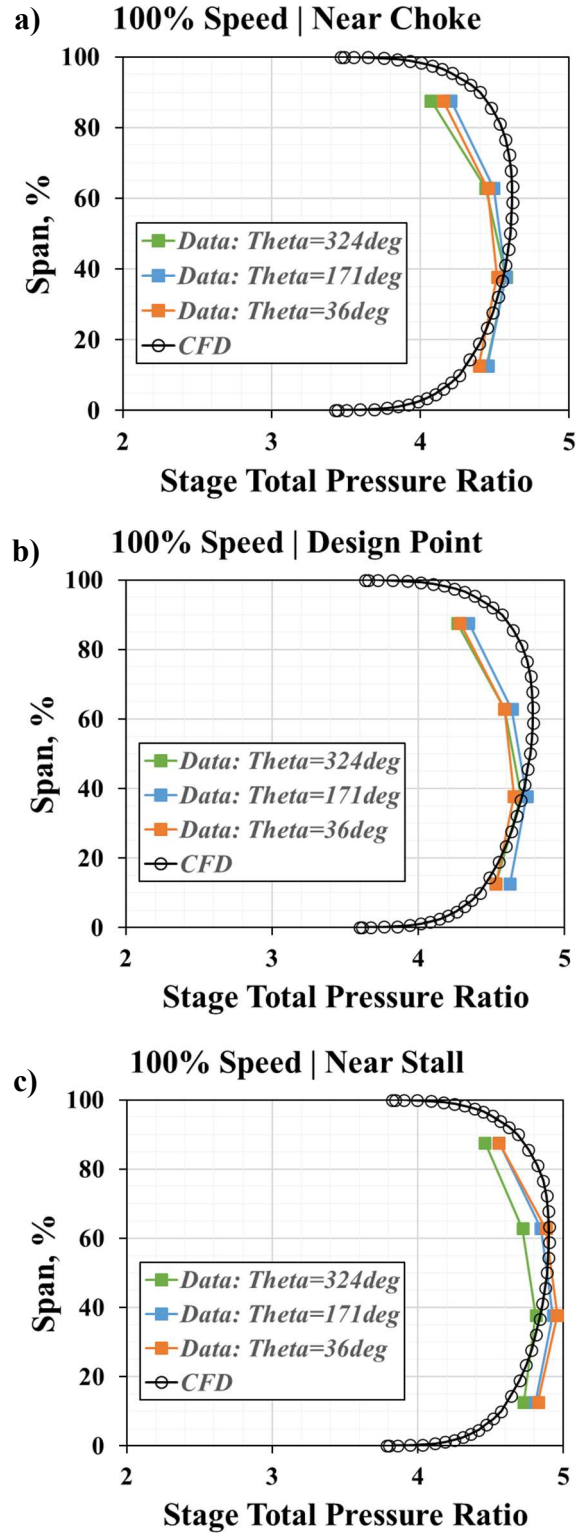**FIGURE 9. IMPELLER EXIT TPR PROFILE AT A) NEAR CHOKE, B) DESIGN POINT AND C) NEAR STALL.**

FIGURE 10. STAGE TPR PROFILE AT A) NEAR CHOKE, B) DESIGN POINT AND C) NEAR STALL.
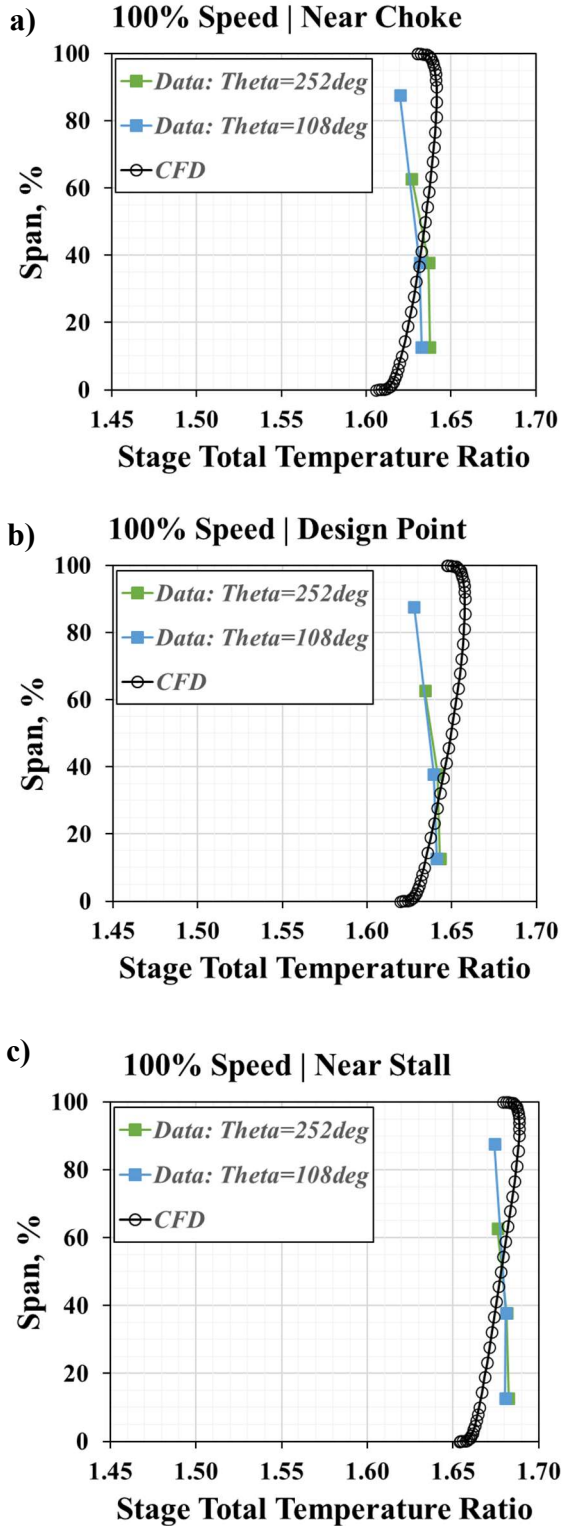
a) 100% Speed | Near Choke

b) 100% Speed | Design Point

c) 100% Speed | Near Stall

FIGURE 11. STAGE TPR AT A) NEAR CHOKE, B) DESIGN POINT AND C) NEAR STALL.

5.3 Spanwise Profiles at Off-Design Conditions

Further validations of the spanwise profiles were conducted at off-design speeds. The comparisons were conducted at the design point for 95% and 90% speeds. The experimental inlet corrected flow rates for the points were 9.80lb$_m$/sec and 9.08lb$_m$/sec, respectively. The corresponding CFD simulations used in the comparison had inlet corrected flow rate values of 9.88lb$_m$/sec and 9.04lb$_m$/sec, respectively.

As can be seen in Figure 12, the comparisons to data again show that even at off design speeds the model still accurately predicts the shape and magnitude of impeller exit TPR. Comparisons of stage TPR and TTR showed similar conclusions as those seen at 100% speed where the magnitude change was accurately predicted but the shape had an opposite trend in the bias.
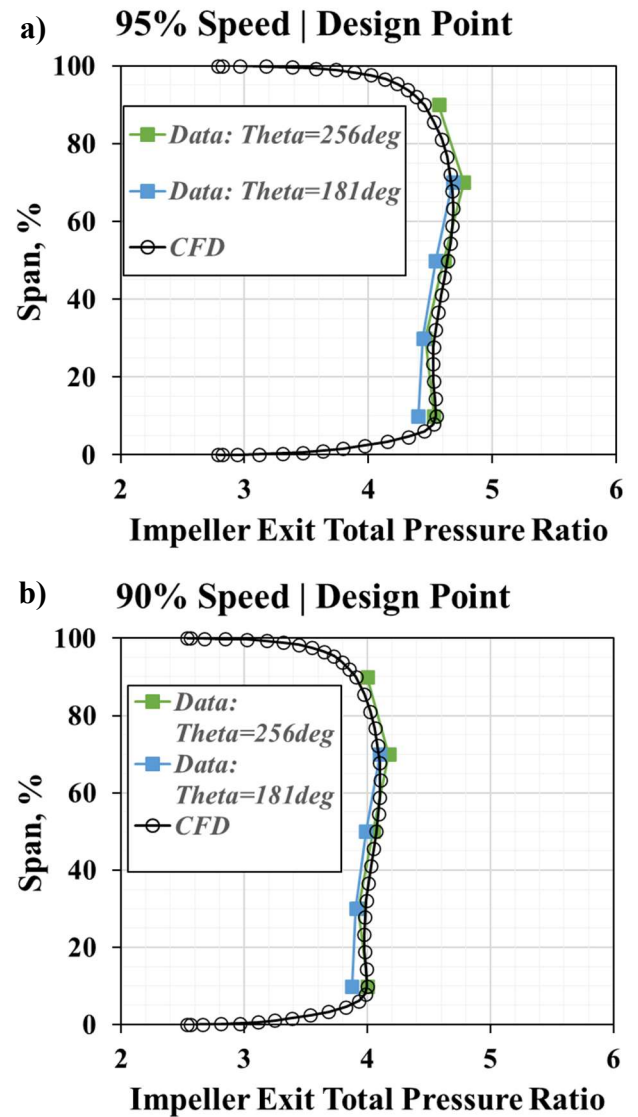

a) 95% Speed | Design Point

b) 90% Speed | Design Point

FIGURE 12. IMPELLER EXIT TPR AT A) 95% SPEED, B) 90% SPEED.

6. IMPELLER FLOW FEATURES

Having extensively validated the numerical model against the experimental results, the model can be used to interrogate the flow field of the HECC impeller alongside the experimental data.

The impeller blade loading at 70% span, 100% corrected speed, and design mass flow rate is presented in terms of the static pressure and isentropic relative Mach number in Figure 13. The main blade operates at incidence approximately appropriate for the design mass flow rate at 70% span, and the loading is fairly uniform along the blade chord, though the work done by the main blade increases in the final 50% of the meridional distance as the centrifugal effect starts to take effect. The exception to the uniformity, however, occurs at 20% of the main blade meridional distance where the leading edge of the splitter blade is located. The splitter blade incidence is more positive at the leading edge than the incidence at the main blade leading edge, and the presence of the splitter blade leading edge results in a localized nearly favorable pressure gradient on the main blade pressure surface, Figure 13. Additionally, the splitter blade loading is less than the main blade loading for almost the entirety of the chord. The local acceleration on the suction surface can be directly observed in the surface isentropic Mach number (calculated using surface static pressure and a reference circumferentially averaged total pressure value at the corresponding radial plane at the inlet), as well as the difference in loading between the main blade and splitter blade. The static pressure and isentropic Mach numbers together indicate that the splitter blade impedes the work done by the main blade and also does not achieve an equal distribution of work in the latter half of the chord.

The influence of the splitter blade leading edge on the main blade pressure surface can be observed via the contour of static pressure through the impeller passage, Figure 14. Due to the positive incidence at the splitter leading edge, the flow accelerates towards the splitter suction side and reduces the static pressure across the passage enough to influence the loading on the main blade suction surface. Moreover, the acceleration results in a separated secondary flow that dominates the splitter-suction-side/main-pressure-side passage, Figure 15. The low momentum region, indicated by the lower relative Mach number in blue, propagates through the passage and likely contributes to the lower loading on the splitter blade observed in Figure 13. The differences between the main-blade/splitter-blade and splitter-blade/main-blade passages shown in Figure 15 are also quite notable. The flow exiting on the pressure side of the splitter blade is more uniform than on the suction side. The differences between the passages, as well as the effect of the splitter blade on the main blade, will be analyzed in a detailed discussion of the HECC impeller geometry in Part II.
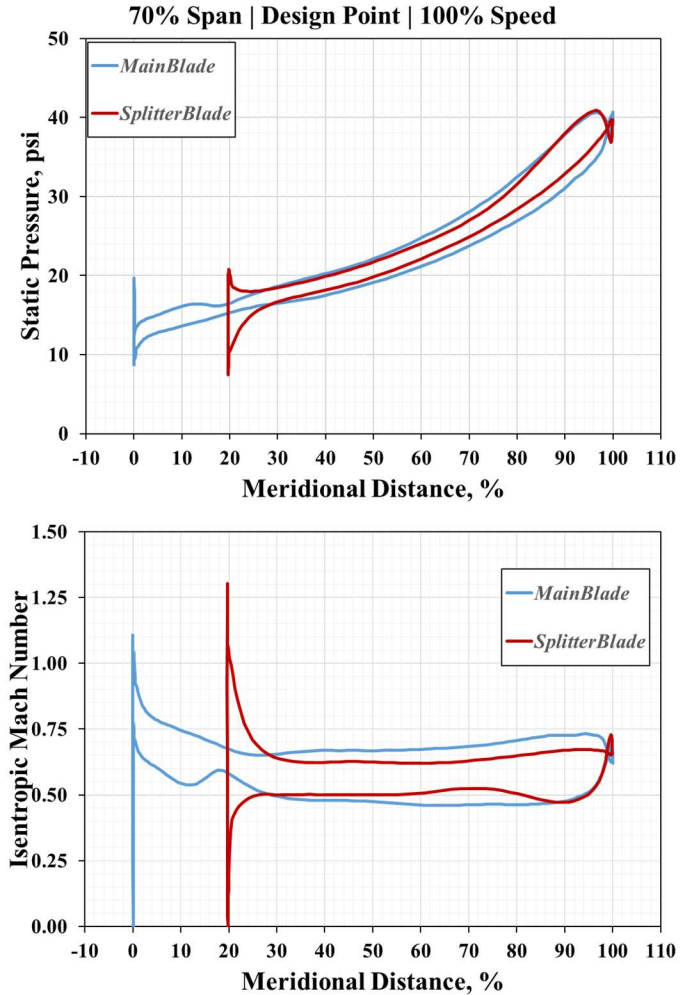

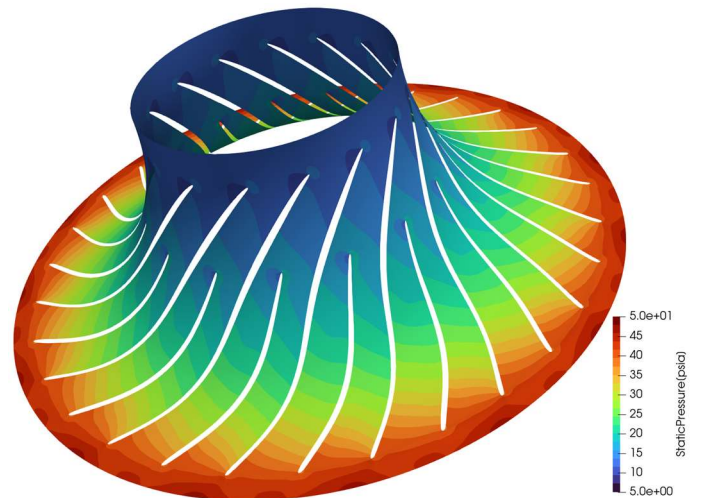FIGURE 13. STATIC PRESSURE LOADING AT 70% SPAN FOR THE 100% DESIGN SPEED DESIGN POINT.

FIGURE 14. STATIC PRESSURE CONTOUR AT 70% SPAN OF THE 100% SPEED DESIGN POINT.
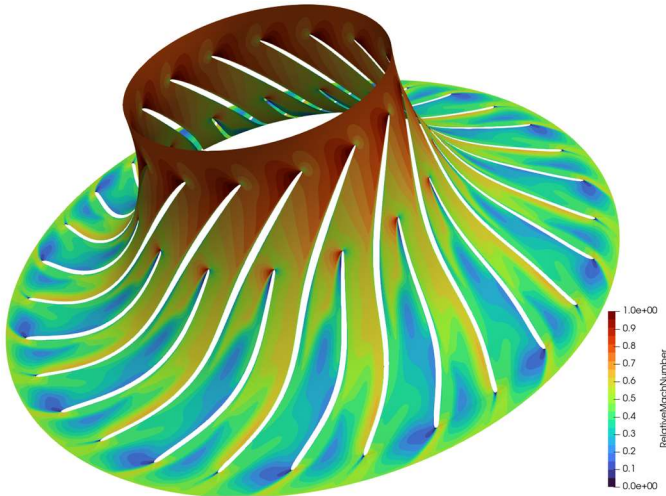
FIGURE 15. RELATIVE MACH NUMBER CONTOUR AT 70% SPAN OF THE 100% SPEED DESIGN POINT.

7. CONCLUSIONS

A detailed validation effort was undertaken as the first part of a multi-part investigation. The validation effort compared a numerical model of the HECC vaneless diffuser configuration model to experimental data published by Harrison et al [1]. The validation effort first focused on establishing a mesh density that reached mesh convergence. Four mesh levels were assessed by running an 8-point speedline for each level. The major compressor performance metrics of total pressure ratio, total temperature ratio, and efficiency reached convergence at all considered operating conditions on the 100% speedline by the fine mesh.

The fine mesh was then used for validation of the model such that it could be used to interrogate the HECC impeller flow field with a high degree of confidence for the remainder of the investigation. A detailed comparison was performed against experimental speedline measurements at station 3 and station 7 at design and off-design speeds from 90% to 100% corrected speed. Good agreement was found in regard to the shapes and magnitudes of all the speedlines that were compared. The model accurately predicted the pressure rise and temperature rise across the machine for all three speeds. The prediction of the stage efficiency was less accurate, as is typical for numerical models of turbomachinery, but considered well within the bounds of acceptable for the uses of the numerical model in the present work.

After validation of the overall performance of the stage and impeller, spanwise profiles were used to ensure the model accurately represented the details of the flow within the stage. At 100% design speed three points were selected: near choke, design point, and near stall. These points were then used to compare profiles for three properties at two different experimental stations (station 3 and station 7). The properties were impeller exit total pressure ratio, stage pressure ratio, and stage temperature ratio. The results showed that the model accurately captured the changes in the impeller exit total pressure ratio shape and magnitude of the profiles as the performance moved from choke to stall. Differences were observed in the stage total pressure ratio and stage total temperature ratio in regard to the bias of the shape. Nonetheless, the spanwise profiles to show good predictions in the magnitude of the stage properties. Further comparisons were done at off-design conditions. The profile comparison was extended to compare the design point for different design speeds. These comparisons showed that the model accurately captured the shape and magnitude changes in impeller exit total pressure ratio across different speeds. The stage properties at different speed captured the change in magnitude well but showed a difference in the shape. With acceptable agreement found between the spanwise measurements and the results predicted by the experiment, the model was deemed acceptable for use in interrogation of the HECC impeller flow.

After the model was fully validated, the numerical solution was used for initial analysis of the impeller flow. At the design mass flowrate at 100% corrected speed, the splitter blade incidence was notable positive. Acceleration of the flow around the splitter blade leading edge caused a localized reduction in work input on the main blade at the meridional chord location where the splitter leading edge is located. The acceleration was then observed to contribute a low momentum flow region that dominates the passage on the suction side of the splitter blade, and correspondingly, significant differences in the flow field between the two impeller passages.

With extensive validation of the numerical model complete, the model will be used in Part II of this investigation to understand the effect of the splitter blade geometry on the overall impeller performance. In Part III, experimental and numerical results will be considered together to evaluate the effect of the impeller tip clearance flow and both the performance and loss generation of the impeller.

REFERENCES

[1] Harrison, H. M., McNichols, E. O., and Blaha, M. R., 2023, "NASA Small Engine Components Compressor Test Facility: High Efficiency Centrifugal Compressor Vaneless Diffuser and Transition Duct Configurations," *Boston, MA*, American Society of Mechanical Engineers Digital Collection, GT2023-103128.

[2] Medic, G., Sharma, O. P., Jongwook, J., Hardin, L. W., McCormick, D. C., Cousins, W. T., Lurie, E. A., Shabbir, A., Holley, B. M., and Van Slooten, P. R., 2017, High Efficiency Centrifugal Compressor for Rotorcraft Applications, E-18856-1.

[3] Harrison, H. M., 2022, "NASA HECC Data Archive," NASA [Online]. Available: https://storage.googleapis.com/hecc-data/NASA-HECC-Data-Archive.zip.

[4] Ni, R. H., 1982, "A Multiple-Grid Scheme for Solving the Euler Equations", AIAA 81-1025R

[5] Evans, S., Yi, J., Nolan, S., Joseph, L., Ni, M., Kulkarni, S., 2021, "Modeling of Axial Compressor With Large Tip Clearances", GT2020-14496

[6] Robles Vega, G., Lee, D. Y., Ni, M., Ni, R. H., 2023, "Part I: Validation and Verification of CFD Analysis for NASA SDT Transonic Fan Stage Test Rig", GT2023-103856

[7] Lee, D. Y., Robles Vega, G., Ni, M., Ni, R. H., 2023, "Part II: Validation and Verification of CFD Analysis for NASA SDT Transonic Fan Stage Coupled with Nacelle", GT2023-103871

[8] Ni, M., Ni, R.H. and Clark, J., 2023,"Les Modeling of High-Lift High-Work LP Turbine Profiles: Part I: Approach", GT2023-102605

[9] Kerestes, J., Marks, C., Clark, J., Wolff, M., Ni, R., Fletcher, N., 2023, "LES Modeling of High-Lift High-Work LPT Blades: Part II-Validation and Application", GT2023-101950

[10] Ni, R. H., Humber, W., Fan, G., Clark, J. P., Anthony, R. J. and Johnson, J. J., 2013, "Comparison of Predictions from Conjugate Heat Transfer Analysis of a Film-Cooled Turbine Vane to Experimental Data", GT2013-94716, ASME J Turbomach

[11] Ni, R. H., Humber, W., Ni, M., Capece, V. R., Ooten, M. and Clark, J., 2016, "Aerodynamic Damping Predictions for Oscillating Airfoils in Cascades Using Moving Meshes", GT2016-57017, ASME J Turbomach

[12] Wilcox, D. C., 1993, "Turbulence Modeling for CFD"